

Particle Simulation of Vibrated Gas-Fluidized Beds of Cohesive Fine Powders

Sung Joon Moon, I. G. Kevrekidis, and S. Sundaresan*

*Department of Chemical Engineering, Program in Applied and Computational Mathematics,
Princeton University, Princeton, New Jersey 08544*

We have used three-dimensional particle dynamics simulations, coupled with volume-averaged gas phase hydrodynamics, to study vertically vibrated gas-fluidized beds of fine, cohesive powders. The volume-averaged interstitial gas flow is restricted to be one-dimensional (1D). This simplified model captures the spontaneous development of 1D traveling waves, which corresponds to bubble formation in real fluidized beds. We have used this model to probe the manner in which vibration and gas flow combine to influence the dynamics of cohesive particles. We have found that, as the gas flow rate increases, cyclic pressure pulsation produced by vibration becomes more and more significant than direct impact, and in a fully fluidized bed, this pulsation is virtually the only relevant mechanism. We demonstrate that vibration assists fluidization by creating large tensile stresses during transient periods, which helps break up the cohesive assembly into agglomerates.

1. Introduction

It is well-known that fine, cohesive particles cannot be fluidized easily.^{1,2} When fluidization by an upflow of gas is attempted, assemblies of such particles have a tendency to lift up as a plug and only form ratholes and cracks through which the fluid escapes. Attractive interparticle forces frequently arise, as a result of capillary liquid bridges or van der Waals forces. A variety of techniques to achieve smooth fluidization of such particles has been explored in the literature. When the cohesion arises from van der Waals forces, as in the case of Geldart type C particles, which are typically 30 μm or smaller in size,¹ coating with hard nanoparticles³ or an ultrathin film⁴ can weaken the attraction between the bed particles, thus enabling smooth fluidization. Alternate approaches to facilitate fluidization include causing agglomerate breakup through a secondary supply of energy using mechanical vibration,^{5–12} acoustic waves,^{13–15} or an oscillating magnetic field.¹⁶ Such approaches have been shown to be effective, even for beds of nanoparticles.¹¹ In the present study, we are concerned with some aspects of the mechanics of vibrated fluidized beds of cohesive particles.

Vibrated layers of granular materials have been studied extensively in the literature, and the formation of patterns in shallow granular layers is now well-known.^{17,18} Mixing and segregation in such vibrated beds have also received considerable attention.^{19–21} The motion of large intruders in vibrated beds, leading to the well-known Brazil nut and reverse Brazil nut effects,^{19,22} has also received much attention in the literature, where experimental measurements suggest a non-negligible influence of the interstitial gas on the observed flow patterns.^{23,24} Generally, the deeper the bed and/or the smaller the bed particles, the greater the influence of the interstitial gas phase on the dynamics of the assembly of particles.

In vibrated fluidized beds, where vibration is supplemented with a fluidizing gas flow (or vice versa), the importance of the interstitial gas is obvious, because the drag that is due to the gas flow supports a substantial portion of the weight of the particles. Vibrated fluidized beds have found many applications in industrial practice (e.g., see an article by Squires²⁵). Understanding the manner in which the vibration aids the fluidization process is important both for macroscopic analysis of vibrated

fluidized beds and for detailed interrogation of agglomerate size distribution and mixing at the agglomerate and particle scales.

Predicting the minimum fluidization velocity of a vibrated fluidized bed (of cohesive particles) is perhaps the simplest quantitative, macroscopic analysis problem one can think of. This indeed has been the subject of many investigations,^{7–9,11,26–29} and different approaches have been proposed in the literature to incorporate the effect of vibration on the overall force balance used to determine the minimum fluidization velocity. Masters and Rietema²⁶ suggested that additional terms must be included in the force balance relation, to account for the increased pressure drop due to cohesion. They included additional terms for interparticle forces, as well as wall friction. Liss et al.²⁷ proposed an additional term to account for the effect of cohesion arising from liquid bridges. Wank et al.⁸ showed that the agglomerate size decreases as the vibration intensity increases, and they studied the effect of the pressure on the minimum fluidization velocity. Erdész and Mujumdar²⁸ developed a theory that includes the effect of vibration in the prediction of the minimum fluidization velocity; they found that the pressure drop decreased as the vibration intensity in their experiments increased with various particles in the size range of 0.15–2.75 mm. However, Tarisin and Anuar²⁹ found the opposite trend in their study of vibrofluidization of particles of 1–34 μm , and others^{7,9,11} found no appreciable dependence on the vibration intensity with particles ranging in size from 12 nm to 100 μm .

Such conflicting reports stem from our limited understanding of the manner in which the vibrating boundary interacts with the assembly of particles in the bed. One can readily envision at least two modes of interaction: (a) when the effect of the interstitial gas on particle motion is of negligible importance, the vibrating base plate clearly imparts impulse to the particle assembly periodically only through direct collisions; and (b) when gas-particle drag is non-negligible, a periodically varying pressure field can be expected to develop in the bed, and the base plate interacts with the bed particles indirectly by driving these pressure pulsations as well. The relative importance of these two contributions can be expected to be dependent on the bed depth, the particle size, and the superficial velocity of the fluidizing gas; however, quantitative estimates are unavailable.

At a more detailed level, it is readily apparent that vibration results in the formation of small agglomerates, which are more

* To whom correspondence should be addressed. Tel.: 609-258-4583. Fax: 609-258-0211. sundar@princeton.edu.

amenable to fluidization; yet, how such small agglomerates are formed is not understood. A clear understanding of this mechanism is an important first step in any effort to capture the effect of vibration on the dynamics of agglomerates (e.g., in a population-balance-type model for vibrated fluidized beds). At first glance, one may speculate that vibration drives vigorous collisions between agglomerates, which, in turn, causes their breakup; however, it is not known if this is, indeed, the dominant mechanism.

In the present study, we have examined the interaction of the vibrating base plate with a bed of particles through detailed simulations. We will demonstrate that (i) as the fluidizing gas velocity is increased, the interaction with the boundary through pressure pulsation becomes more and more dominant, and (ii) above the minimum fluidization conditions, the interaction occurs almost exclusively through pressure pulsations. We will also show that the large tensile stress induced by the vibration is a more important mechanism (than vigorous collisions between agglomerates) in causing the breakup of the cohesive particle assembly.

The dynamic behavior of gas-fluidized beds containing a large number of particles has been widely examined in the literature through two-fluid models.^{30–32} This approach requires closure relations for gas–particle interactions and the stresses. Considerable progress has been made in developing and validating the closures for assemblies of noncohesive particles,^{30–32} but not for the case of cohesive materials. Accurate two-fluid model boundary conditions that capture the effect of vibrating boundaries are also unavailable. Furthermore, the two-fluid model approach is not well-suited for investigation of the mechanism of agglomerate breakup. For these reasons, we model vertically vibrated gas-fluidized beds of fine powders using a hybrid scheme, where the solid phase is treated as discrete spherical particles, following the so-called discrete element method (DEM, or soft-sphere molecular dynamics),³³ whereas the gas phase is treated as a continuum, following the volume-averaged hydrodynamics, just as in a two-fluid model.^{31,32} This DEM-based hybrid approach was proposed by Tsuji et al.³⁴ in their simulation of two-dimensional (2D) fluidized beds, and it has been subsequently refined by others.^{35,36} Recently, this model has been used to study fluidized beds of Geldart A particles,³⁷ the effect of an arbitrary cohesive force that is proportional to the particle buoyant weight,^{38,39} and segregation in fluidized beds of bidisperse particles.⁴⁰

Even with the high-speed computing that is available today, one can only simulate small systems, which are orders of magnitude smaller than real vibrated fluidized beds, through this hybrid approach. Therefore, it is essential that one choose suitable, idealized problems to probe the underlying mechanics. With this in mind, we have chosen essentially one-dimensional (1D) vibrated fluidized beds of particles, applying periodic boundary conditions in the two lateral directions. This limits the macroscopic dynamics to the vertical direction only, and one obtains one-dimensional traveling waves (1D-TW) instead of bubblelike voids observed in experiments and in fully three-dimensional flow simulations; nevertheless, such an idealized problem is, in our opinion, adequate to expose the manner in which the vibrating base plate interacts with the bed particles and how dense cohesive regions are broken down into smaller agglomerates.

The rest of the paper is organized as follows. The DEM-based hybrid model is described in section 2, and bubble formation, realized as 1D-TW in our geometry (narrow cross-sectional areas), is presented in section 3.1. The effect of

cohesion and vibration on the fluidization is presented in section 3.2, and the manner in which the vibration enhances the fluidization will be discussed in section 3.3. The pressure drop in vibrated fluidized beds and the mechanism through which the vibration breaks up cohesive assemblies will be presented in sections 3.4 and 3.5, respectively, which are followed by the conclusions in section 4.

2. Method: Discrete Element Method (DEM)-Based Hybrid Model

Since its introduction by Cundall and Strack³³ almost three decades ago, the DEM has been successfully used in modeling various particulate flow problems, including hopper flows,⁴¹ shearing cells,⁴² rotating drums,⁴³ and oscillated layers.^{44,45} Comprehensive description of this method can be found in the literature.^{46–48} Below, we briefly describe the main idea of the DEM, and subsequently focus on how the volume-averaged gas-phase hydrodynamics is coupled with the individual particle dynamics in our model.

2.1. Discrete Element Method (DEM). In the DEM simulation, particles are modeled as “soft” spheres (the deformation taken into account by overlaps), whose trajectories are computed by integrating Newton’s equations of motion. When objects (particles or system boundaries) come into contact, the interaction is resolved by decomposing the interaction force into the normal and tangential directions, relative to the displacement vector between the objects at contact ($\mathbf{F}_{\text{cont}} = (\mathbf{F}_n, \mathbf{F}_s)$), and the energy dissipation upon contact is characterized by the inelasticity and the surface friction. We use the so-called spring-dashpot model, with a Hookean spring.³³ The objects are allowed to overlap upon contact, and the contact force in the normal direction (\mathbf{F}_n) is determined by the amount of overlap (Δ_n) and the normal component of the relative velocity at contact v_n :

$$\mathbf{F}_n = (k_n \Delta_n - \gamma_n v_n) \hat{\mathbf{n}} \quad (1)$$

where k_n is the spring stiffness in the normal direction, γ_n the damping coefficient, and $\hat{\mathbf{n}}$ the unit vector in the normal direction at contact, pointing from the contact point toward the particle center. The damping coefficient γ_n is related to k_n by the normal coefficient of restitution e ($0 \leq e \leq 1$):

$$\frac{4k_n/m^*}{(\gamma_n/m^*)^2} = 1 + \left(\frac{\pi}{\log e} \right)^2 \quad (2)$$

where $1/m^* = 1/m_i + 1/m_j$, and i and j are indices of interacting particles or objects. In principle, the value of k_n is determined by the Young’s modulus of the material under consideration. However, unless stated otherwise, we use a much smaller value for k_n , compared to that computed based on the usual range of Young’s modulus. If the main results are not qualitatively different, it is favorable to use a smaller value of k_n , because the collision duration time in DEM scales with $k_n^{-1/2}$, which determines the integration time-step size required to accurately resolve the interaction during the contact. This is a well-known issue in DEM simulations.^{46,47} We varied k_n over 3 orders of magnitude and verified that the main results are not dependent sensitively on the choice of k_n , even though the actual contact force between the objects certainly is dependent on the value of k_n . For instance, the results for two k_n values differing by a factor of 10 will be presented in Figures 7–9 later in this paper.

The interaction in the tangential direction is modeled by a “spring and slider”, and the contact force is given by

$$\mathbf{F}_s = -\text{sign}(v_s) \times \min(k_t \Delta_s, \mu |\mathbf{F}_n|) \hat{\mathbf{s}} \quad (3)$$

where v_s is the tangential component of the relative velocity at contact ($v_s = \mathbf{v}_s \cdot \hat{\mathbf{s}}$, where $\mathbf{v}_s = \hat{\mathbf{n}} \times (\mathbf{v}_{ij} \times \hat{\mathbf{n}})$ and $\hat{\mathbf{s}}$ is the unit vector in the tangent plane collinear with the component of the relative velocity at contact), k_t the tangential spring stiffness that is related to k_n by the Poisson’s ratio of the material ν_p ($k_t = 2k_n(1 - \nu_p)/(2 - \nu_p)$), and Δ_s is the magnitude of tangential displacement from the initial contact. The magnitude of the total tangential force is limited by the Coulomb frictional force $\mu |\mathbf{F}_n|$, where μ is the coefficient of friction. More sophisticated and/or realistic interaction models, such as that of Walton and Braun’s model⁴⁹ or a Hertzian spring-dashpot model,⁵⁰ may also be used. However, we choose a simple Hookean spring-dashpot and spring-slider model, because it has been shown to successfully reproduce many experimental observations,^{41,43,45} and it is computationally more tractable than others.

Among different interparticle forces, other than those due to contact, we consider only cohesion that results from van der Waals forces. In principle, the cohesion can be dependent on the particle characteristics, such as polarizability, particle size, and asperity.⁵¹ However, we adopt a simple formula by Hamaker, because we intend to determine the effect of cohesion on the fluidization behavior, rather than to validate different cohesion models. Particulate flows in industry often consist of particles with a wide range of sizes and shapes; however, we seek a better understanding of simple systems that consist of monodisperse spheres, which are well-characterized by a small set of parameters. The cohesive van der Waals force between two spheres of radii r_i and r_j can be expressed as⁵¹

$$\begin{aligned} \mathbf{F}_c &= -\frac{A}{3} \frac{2r_i r_j (s + r_i + r_j)}{[s(s + 2r_i + 2r_j)]^2} \times \\ &\quad \left[\frac{s(s + 2r_i + 2r_j)}{(s + r_i + r_j)^2 - (r_i - r_j)^2} - 1 \right] \hat{\mathbf{n}} \\ &\approx -\frac{A}{12} \left(\frac{r}{s^2} \right) \hat{\mathbf{n}} \quad (\text{for } r = r_i = r_j \text{ and } s \ll r) \end{aligned} \quad (4)$$

where A is the Hamaker constant and s is the intersurface distance. Because the original formula is a rapidly decreasing function of s , further simplification using the assumption of $s \ll r$ has been made. This model has a singularity at contact. To avoid this artifact, we introduce a widely accepted minimum cutoff value for the intersurface distance of 0.4 nm ($\equiv \delta^*$), which corresponds to the intermolecular center-to-center distance.⁵² In what follows, the level of cohesion is represented by the cohesive Bond number Bo , which is defined as the ratio of the maximum cohesive force (at the minimum cutoff separation δ^*) to the particle weight. Other types of cohesion can be readily taken into account in DEM-based models.^{39,53,54}

2.2. Coupling with Gas-Phase Hydrodynamics. The dynamics of individual particles is coupled with the volume-averaged gas-phase hydrodynamics.³⁴ In this hybrid model, the equations of motion for individual particles have two additional terms (compared to traditional DEM modeling particles under vacuum) arising from the presence of the gas phase:

$$m_p \frac{d\mathbf{v}_p}{dt} = m_p \mathbf{g}_{\text{eff}} + \mathbf{F}_{\text{cont}} + \mathbf{F}_c + \frac{V_p}{\phi} \beta(\phi)(\mathbf{u}_g - \mathbf{v}_p) - V_p \nabla p \quad (5)$$

where m_p and \mathbf{v}_p are individual particle mass and velocity, respectively. The first term on the right-hand side represents the body force due to gravity, and \mathbf{g}_{eff} is the effective gravitational acceleration in the reference frame where equations are integrated. For nonvibrated beds, \mathbf{g}_{eff} is simply the gravitational acceleration \mathbf{g} . When the bed is subject to a single frequency oscillation, the equations are integrated in the vibrated frame, and $\mathbf{g}_{\text{eff}} = \mathbf{g}[1 + \Gamma \sin(2\pi f t)]$, where Γ is the maximum acceleration of the base plate (distributor) nondimensionalized by the gravitational acceleration ($\Gamma = A_p(2\pi f)^2/g$, where $g = |\mathbf{g}|$, A_p is the oscillation amplitude, and f is the oscillation frequency). We assume the oscillating base plate is comprised of the same materials as the particles (the same values for e and μ), and that the mass of the plate is infinitely large, compared to that of an individual particle. The second term and the third term represent the aforementioned contact force and van der Waals force, respectively. The total force acting on the particles due to the fluid is commonly partitioned into the local drag component and the effective buoyant component, as was done here (see, e.g., an article by Ye et al.³⁷). The fourth term accounts for the drag force, and the last term accounts for the contribution of the gradually varying part of the pressure field, where V_p is the volume of each particle; ϕ and \mathbf{u}_g are volume-averaged solid-phase volume fraction and gas-phase velocity, respectively; β is the inter-phase momentum transfer coefficient;³¹ and p is the gas-phase pressure.

Generally, the gas-phase quantities are obtained by simultaneously integrating the coarse-grained mass and momentum balance equations. We assume the gas phase to be incompressible, which will be validated later (see section 3.4). The addition of continuity equations for the gas phase and solid phase reads

$$\nabla \cdot [(1 - \phi)\mathbf{u}_g + \phi\mathbf{u}_s] = 0 \quad (6)$$

and a reduced momentum balance equation for the gas phase, based on generalized Darcy’s law, is given as

$$0 = -(1 - \phi)\nabla p + \beta(\phi)(\mathbf{u}_s - \mathbf{u}_g) \quad (7)$$

where \mathbf{u}_s is the coarse-grained solid phase velocity. Coarse-grained variables are considered only on grids where the continuum balance equations are solved. Note that the solid phase continuum (or coarse-grained) variables are explicitly available in the course of DEM computation.

2.3. Beds of Narrow Cross-Sectional Area. Only beds of narrow cross-sectional areas will be considered, and the volume-averaged gas phase (and, hence, the solid phase coarse-grained variables as well) is assumed to be 1D. However, the solid phase is maintained to be 3D, as the way particles pack and collide in lower dimensions are considerably different from those in realistic 3D cases. Our assumption allows us to consider relatively deep beds (through inexpensive computational effort) and to derive the basic physics of more-complicated dynamics in higher dimensions.

Solid-phase coarse-grained variables at 1D discrete grid points are computed by distributing the particle mass and momenta to the nearest two grid points, using a halo function h that continuously decreases to zero around the particle:

$$h(z - z_0) = \begin{cases} \frac{1 - |z - z_0|}{\Delta z} & (\text{for } |z - z_0| < \Delta z) \\ 0 & (\text{otherwise}) \end{cases} \quad (8)$$

where z is the particle position in the vertical direction, z_0 is the position of a neighboring grid point, and Δz is the grid

D

spacing. It is readily seen that h has the property that the particle quantities are distributed to the two nearby grid points, inversely proportional to the distance to the grid point. The coarse-grained variables, the number density n and \mathbf{u}_s , on the grids are then defined simply as

$$n(z_0) = \sum_{i=1}^N h(z_i - z_0) \quad (9)$$

$$n(z_0)\mathbf{u}_s(z_0) = \sum_{i=1}^N h(z_i - z_0)\mathbf{v}_{p,i} \quad (10)$$

where z_i and z_0 are the i th particle location and nearby grid location, respectively.

The assumption of the gas phase to be 1D facilitates further mathematical simplifications of the above particle–gas interaction formulation. In 1D continuum cases, eq 6 can be integrated:

$$(1 - \phi)\mathbf{u}_g + \phi\mathbf{u}_s = \mathbf{U}_s \quad (11)$$

where \mathbf{U}_s is the superficial gas flow velocity. Strictly speaking, in a vibrated fluidized bed, \mathbf{U}_s may also vary periodically. The extent of its variation will be dependent on the dynamics of the gas in the plenum and the flow resistance offered by distributor (base plate). One can show that the temporal variation of \mathbf{U}_s will be small for a highly resistive distributor plate, which we assume. Thus, in the modeling of both nonvibrated and vibrated fluidized beds, \mathbf{U}_s will be considered to be a time-independent parameter.

After some manipulation, eq 5 can be rewritten as follows:

$$m_p \frac{d\mathbf{v}_p}{dt} = m_p \mathbf{g}_{\text{eff}} + \mathbf{F}_{\text{cont}} + \mathbf{F}_c + \frac{V_p}{\phi} \beta(\phi) \times \left[(\mathbf{u}_s - \mathbf{v}_p) - \frac{1}{(1 - \phi)^2} (\mathbf{u}_s - \mathbf{U}_s) \right] \quad (12)$$

Note that the presence of the gas phase is realized as additional terms involving coarse-grained variables, instead of separate continuum equations to be integrated simultaneously. In the course of integration, ϕ and \mathbf{u}_s in eq 12 must be evaluated at the particle location, rather than at the grid points. We evaluate them by linearly interpolating those values at the neighboring grid points.

For the interphase momentum transfer coefficient β , we use an expression proposed by Wen and Yu:⁵⁵

$$\beta = \frac{3}{4} C_D \frac{\rho_g \phi (1 - \phi) |\mathbf{u}_g - \mathbf{u}_s|}{d_p} (1 - \phi)^{-2.65} \quad (13)$$

where C_D is the drag coefficient, ρ_g is the gas-phase mass density, and d_p is the particle diameter. The drag coefficient proposed by Rowe⁵⁶ is used in our model:

$$C_D = \begin{cases} \frac{24}{Re_g} (1 + 0.15 Re_g^{0.687}) & (\text{for } Re_g < 1000) \\ 0.44 & (\text{for } Re_g \geq 1000) \end{cases} \quad (14)$$

where

$$Re_g = \frac{(1 - \phi) \rho_g d_p |\mathbf{u}_g - \mathbf{u}_s|}{\mu_g} \quad (15)$$

and μ_g is the gas-phase viscosity. Because we consider fine

Table 1. Parameter Values Used in This Work

parameter	typical values for dimensional quantities	nominal values for dimensionless parameters
μ_g	$1.8 \times 10^{-4} \text{ g/(m s)}$	
g	981 cm/s^2	
d_p	$50 \text{ }\mu\text{m}$	
ρ_s	0.90 g/cm^3	
$\sqrt{gd_p}$	2.2 cm/s	
$\sqrt{d_p/g}$	$2.3 \times 10^{-3} \text{ s}$	
δ	$0.4 \text{ nm} (= \delta^*)$	8.0×10^{-6}
Δt	$5.6 \times 10^{-7} \text{ s}$	2.5×10^{-4}
$\Delta z/d_p$		1.5
ϵ		0.9
μ		0.1
k_n		$2.0 \times 10^5 - 2.0 \times 10^6$
v_p		0.3
Γ		0–10
f	less than $\sim 100 \text{ Hz}$	0–0.25

powders, Re_g is generally small, and we use the assumption $Re_g \ll 1$, which further simplifies β :

$$\beta(\phi) = 18 \frac{\mu_g}{d_p^2} \phi (1 - \phi)^{-2.65} \quad (16)$$

Casting eqs 12 and 16 in a dimensionless form, using ρ_s , d_p , $\sqrt{gd_p}$, $\sqrt{d_p/g}$ as the characteristic density, length, velocity, and time, respectively, one obtains the following nondimensional groups (arrows indicate changes in the notation from dimensional variables to nondimensional variables that will be used henceforth):

$$\text{for spring stiffness: } k_n \leftarrow \frac{k_n}{\rho_s g d_p^2}$$

$$\text{for superficial gas flow rate: } U_s \leftarrow \frac{U_s}{\sqrt{gd_p}}$$

$$\text{for scaled minimum separation distance: } \delta \equiv \frac{\delta^*}{d_p}$$

$$\text{for the cohesive bond number: } Bo \equiv \frac{A}{4\pi \rho_s g d_p^2 \delta^2}$$

$$\text{for the Stokes number: } St \equiv \frac{\rho_s g^{1/2} d_p^{3/2}}{\mu_g}$$

together with nondimensional parameters, namely Γ , $f \leftarrow f \sqrt{d_p/g}$, e , μ , and v_p . (See the Nomenclature section and Table 1 for a listing of the parameters used in this study.)

3. Results and Discussion

We simulate both nonvibrated and vibrated gas-fluidized beds of noncohesive or cohesive particles ($0 \leq Bo \leq 50$). We consider beds of narrow, square-shaped cross-sectional areas of $5d_p \times 5d_p$ or $10d_p \times 10d_p$ with a static depth of $H_0 \approx 100d_p$ and $H_0 \approx 200d_p$ (which consist of 3000 and 6000 particles, respectively, in beds with a cross section of $5d_p \times 5d_p$). Periodic boundary conditions are imposed in both lateral directions, to avoid strong side-wall effects in beds with such a small aspect ratio. We check that our results are not sensitively dependent on a particular choice of cross-sectional area or the depth of the bed (e.g., see Figure 2). We mostly use a bed with dimensions of $\sim 5d_p \times 5d_p \times 100d_p$ in the following computations, unless otherwise stated. We used values of d_p , $1.5d_p$, and

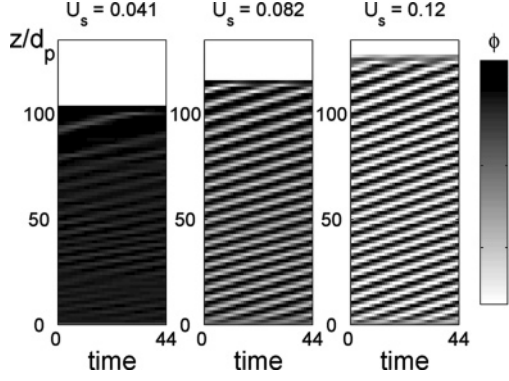


Figure 1. Spatiotemporal plots of conventional fluidized beds of non-cohesive particles ($Bo = 0$, $St = 55$) at three different superficial gas flow rates. Gray scale represents the local volume fraction of particles; both the regions of the minimum value ($\phi \approx 0.33$) in the gray scale bar and the completely void regions ($\phi = 0$) above the bed top surface are shown in the same white color.

$2d_p$ for the grid spacing Δz . The detailed profiles of the coarse-grained variables are slightly dependent on the choice of Δz (the bigger the grid size is, the smoother the variables are, as one can readily expect); however, the main results remain the same, unless the grid size is too large; we set $\Delta z = 1.5d_p$ in all the results presented here. In the following, all the quantities will be shown in nondimensional form.

3.1. Bubbling and One-Dimensional Traveling Waves. We start by considering conventional (nonvibrated) gas-fluidized beds of noncohesive particles to ensure that our model captures basic experimental observations. We first estimate the minimum fluidization velocity through a simulated quasi-static increase in the gas flow rate (from zero) and the measurement of the pressure drop across the bed, which yields $U_{mf} \approx 0.022$. This estimate is slightly smaller than what we can compute using the force balance relation and the approximate formula of Wen and Yu ($U_{mf} \approx 0.023$);⁵⁷ in this calculation, we used a value of $\phi_{mf} = 0.652$, which was measured from the bulk of the bed. When the gas flow rate exceeds U_{mf} , the bed in our model starts to expand inhomogeneously and forms alternating bands of plugs and voids. Particles located at the bottom of one plug “rain down” through a void region and accumulate at the top of the lower plug, causing the void regions to rise to the top in a periodic fashion (Figure 1). This phenomenon corresponds to the formation of a periodic train of bubblelike voids in real fluidized beds, which appears as 1D-TW in the narrow beds we consider. These waves represent the first stage in the bifurcation hierarchy, leading to various inhomogeneous structures in higher-dimensional (i.e., 2D or 3D) fluidized beds.^{58–60} The secondary bifurcations that occur in real fluidized beds are suppressed in our simulations, which are forced to retain the 1D character. As the gas flow rate increases, both the wave speed and amplitude increase (see Figure 1). In the subsequent sections, we will use the 1D-TW as an indicator that characterizes the fluidizability of the bed.

3.2. Cohesion, Vibration, and Fluidization. When the gas flow rate is well above U_{mf} , the bed exhibits clearly visible 1D-TW (for instance, see the cases of $U_s = 0.082$ and 0.12 in Figure 1). In this section, we examine the influence of the cohesion (between particles) on the fluidizability of a bed, and we explore how mechanical vibration facilitates the fluidization of beds of cohesive particles.

Figure 2 shows the effect of Bo on the wave speed, where we have kept $St \approx 55$ and $U_s = 0.12$ (the same values as in the last panel of Figure 1). As Bo increases, the wave gradually slows and eventually disappears. At $Bo = 6$, the wave travels

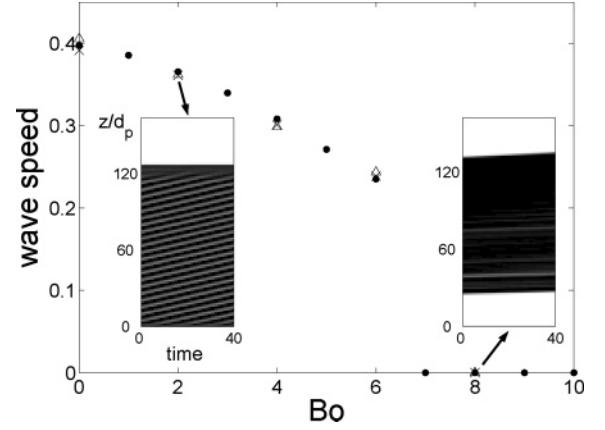


Figure 2. (●) Travelling wave speed (filled circles) in nonvibrated gas-fluidized beds ($\Gamma = 0$), for various levels of cohesion; $U_s = 0.12$. Beds of larger Bo values (more than ~ 6) do not get fluidized; instead, the entire bed moves up as a plug. Insets are spatiotemporal plots of a moderately cohesive bed that is fluidized ($Bo = 2$) and a more cohesive bed ($Bo = 8$) that is not fluidized and rises as a plug at this flow rate. Also shown are data for the wave speeds obtained in beds with dimensions of (Δ) $\sim 5d_p \times 5d_p \times 200d_p$ and (\times) $\sim 10d_p \times 10d_p \times 100d_p$.

intermittently, remaining stationary for some time and traveling at other times, and the wave speed during the nonstationary phase is shown in Figure 2. For $Bo > 7$, the entire bed rises up as a plug at this flow rate, which is consistent with the well-known experimental observations in narrow beds of strongly cohesive particles (see the review article by Sundaresan⁶⁰ and references therein). Further increases of U_s improve the fluidizability of the bed only slightly, confirming that beds of highly cohesive particles cannot be fluidized by simply increasing the gas velocity.

The results shown in Figure 2 are obtained with the assumption that the interaction between the particle and the base plate is noncohesive. We check that the adhesion at the base plate does not make any difference in the above results, as well as all the main results presented here. The only noticeable difference is that strongly cohesive particles at the bottom of a bed become stuck to the plate for some time (during a cycle, in vibrated beds), depending on the oscillation parameters and the superficial gas flow velocity. Detailed comparison between the two cases (with and without adhesion) is shown later in Figure 7.

Now, we subject beds of even more cohesive particles ($Bo = 20$) to mechanical vibration of a single-frequency sinusoidal oscillation in the direction of gravity. When the vibration intensity is strong enough (when Γ exceeds a certain value), even these highly cohesive beds get fluidized in the sense that 1D-TW reappears (Figure 3). At a fixed gas flow rate (we assume it to be time-independent; see the discussion in section 2.3), the wavelength apparently increases with Γ ; however, the wave speed remains almost the same (see Figure 3). We define the critical Bond number Bo_c as the maximum value of Bo for which the bed is fluidizable (generating 1D-TW) at given set of oscillation parameters, and compute it as functions of Γ and f , using a bisection-type search along the Bo -axis. We find that Bo_c increases almost linearly with Γ (Figure 4), but it is only weakly dependent on f (Figure 5). The frequency range shown in this figure corresponds to the usual operation range of 10–100 Hz, for the particle size of $d_p = 50 \mu\text{m}$. In this range of frequencies, Bo_c is virtually independent of the frequency. As the gas flow rate increases, Bo_c slightly increases at fixed values of Γ and f (see the cases for $\Gamma = 3$ and 6 in Figure 4).

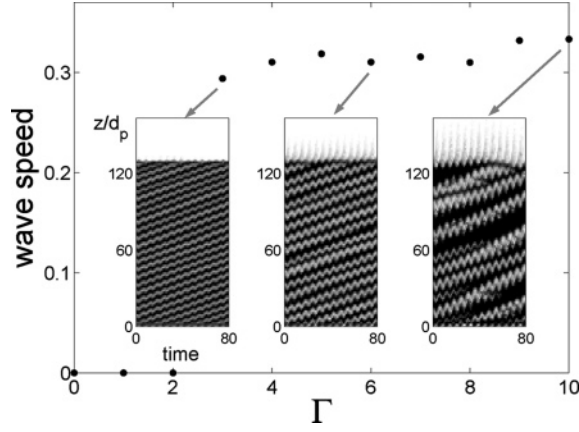


Figure 3. Travelling wave speed in beds of highly cohesive powders ($Bo = 20$) subject to vibrations with various levels of Γ . The traveling wave reappears for $\Gamma > 2$. Insets are spatiotemporal plots of three different cases ($\Gamma = 3.0, 6.0, 10$), shown in the vibrating plate frame; $f = 0.16$, and $U_s = 0.12$.

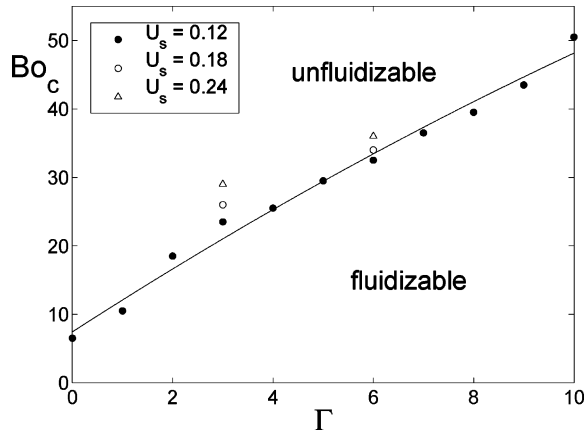


Figure 4. Critical values of Bo , above which the bed does not get fluidized at given vibration parameters, as a function of Γ . Three different levels of U_s are used for $\Gamma = 3.0$ and 6.0 ; $f = 0.16$. A solid line, which represents the least-squares fit for the cases of $U_s = 0.12$, is included to guide the eye.

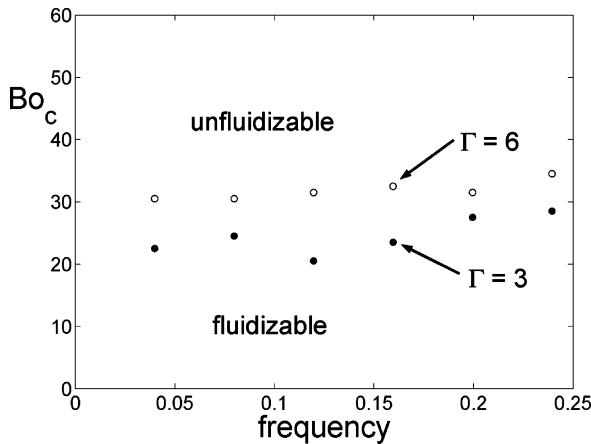


Figure 5. Critical values of Bo as a function of f , for two different levels of Γ . $U_s = 0.12$.

3.3. The Role of Vibration: Direct Impact versus Pressure Pulsation. In this section, we discuss the manner in which the vibrating base plate, or the distributor, interacts with the bed material.

In the absence of gas, the kinetic energy of individual particles in vibrated beds is obtained only from direct impact with the plate and is dissipated through interaction between particles. In

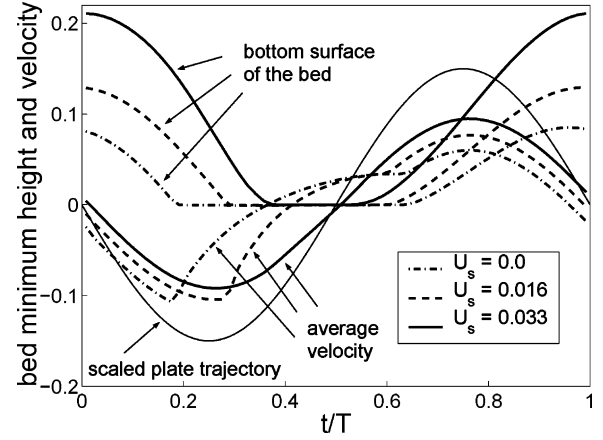


Figure 6. Bottom surface and the average vertical velocity of vibrated beds (averaged over all the particles in the bed) during a cycle, shown in the vibrating frame, obtained for three different gas flow velocities; $Bo = 20$, $\Gamma = 3.0$, and $f = 0.16$. A thin solid line, which represents an arbitrarily rescaled plate trajectory in the laboratory frame, is drawn to represent the phase angle during a cycle.

shallow beds ($H_0 < \sim 20d_p$), the fluctuating kinetic energy (granular temperature) dissipates so quickly through collisions that the entire bed can be well-approximated by one solid body. The dynamics of the center of mass of such a bed can be described by that of single perfectly inelastic ball on a vibrating plate.⁶¹ Vibrated shallow beds in a vacuum undergo period doubling bifurcations as Γ is varied.⁶² Such layers of a large aspect ratio form various spatiotemporal standing wave patterns.^{17,18} However, the temporal dynamics of vibrated deep beds (with a depth of ~ 20 particles or more) under vacuum are not commensurate with the oscillation frequency and they exhibit more complicated nonperiodic behavior.⁶³

When the gas-phase effects are taken into account, the gas drag causes the dynamics of vibrated deep beds to deviate from those under vacuum, and the deviation is more pronounced for smaller particles (because the gas drag is larger). For the deep beds of fine powders considered here, the presence of a gas phase modifies the bed dynamics so that the temporal dynamics become periodic. In the absence of a net flow ($U_s = 0$) the bed lifts off from the plate only slightly (even smaller than the particle size) during a fraction of a cycle, and the bed impacts the plate later in the same cycle (dot-dashed lines in Figure 6). This periodic behavior has the same periodicity as the plate oscillation. Even for higher values of Γ , the period doubling phenomenon, which occurs in vibrated shallow layers under vacuum, is not observed. Note that, in the early phase of the oscillation cycle shown in Figure 6 ($0 < t/T < 0.25$), the plate moves downward (as does the base plate), and yet the bottom surface of the bed is approaching the distributor plate, i.e., the bed is descending faster than the plate. The bed hits the plate, remains in contact for a duration of time, and then detaches from it.

When the gas flow is turned on and its rate is increased, the velocity of the bed (relative to the base plate) during its short flight increases and the bed lifts off further from the plate (Figure 6). The upward gas flow resists the downward motion of the bed; hence, not only the duration of direct impact but also its magnitude (strength) gradually decreases (see the top panel in Figure 7) as the gas flow rate increases. When the adhesion at the base plate is taken into account (dashed lines in Figure 7), the plate experiences some force, even when the bulk of the bed is in flight (for t/T values less than ~ 0.2 or greater than ~ 0.6), because there are a small number of particles stuck to the plate. Other than this, compared to the case when the

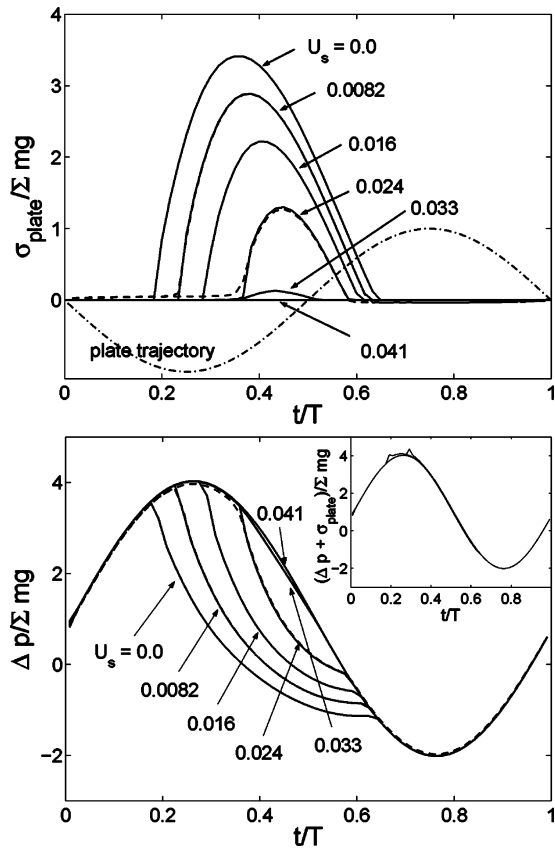


Figure 7. (Top) The normal stress tensor on the base plate, scaled by the bed weight per unit cross-sectional area (Σmg), is shown during a cycle for different superficial gas flow rates; $Bo = 20$, $\Gamma = 3.0$, $f = 0.16$, and $k_n = 2.0 \times 10^5$. Solid lines are obtained by neglecting adhesion at the base plate (Bo_p , the Bo at the plate, is equal to zero). Dashed lines are obtained when the adhesion is taken into account ($Bo_p = 40$), for two cases ($U_s = 0.0082$ and 0.024), which are almost the same as the nonadhesive cases. A dot-dashed line, which represents the plate trajectory in an arbitrary unit, is drawn to represent the phase angle during a cycle. (Bottom) The scaled pressure drop for the same cases as in the top panel are shown. Inset shows the sum of the pressure drop and the normal stress at the base plate for three cases ($U_s = 0.0, 0.016$, and 0.033), all of which virtually coincide with the reduced effective gravity (g_{eff}/g) in the vibrating frame [sinusoidal curve; $1 + \Gamma \sin(2\pi ft)$]. Small excess amounts, appearing as small peaks on top of a sinusoidal curve, arise from the transient restoring force of the soft particles at the impact, which gradually disappears as the plate impacts the bed more gently with increasing U_s (there are no apparent additional peaks for $U_s = 0.033$).

adhesion is neglected (solid lines), no difference is observed. The bed eventually hardly touches the plate at some gas flow rate, above which direct impact remains minimal. It will be shown in the next section that the minimum gas flow rate at which the direct impact virtually vanishes is, for all practical purposes, the same as the minimum fluidization velocity in vibrated beds.

3.4. Pressure Drop in Vibrated Beds. The pressure drop across vibrated beds oscillates with the same periodicity as the plate oscillation (see the bottom panel in Figure 7). The pressure drop increases (decreases) when the base plate moves down (up) (see Figure 6 and the bottom panel in Figure 7, for $t/T < \sim 0.5$). At first glance, this seems to be counter-intuitive, because the pressure drop increases when the plate is “moving away”. However, note that the change in the pressure drop is determined by the change in the gap between the bed and the base plate (i.e., the relative motion, with respect to the plate), not by the absolute motion of the base plate in the laboratory frame. As noted in the previous section, the bed approaches the plate during

the phase of the oscillation cycle when the plate is moving down from its mean position.

As soon as impact occurs, the pressure drop begins to decrease rapidly, even below zero. While the bed is moving away from the plate after the takeoff (see $t/T > \sim 0.6$ in Figure 6), the pressure drop continues to decrease. During this time, a region of lower pressure is being created in the gap between the bed and the plate (see the bottom panel in Figure 7). Our results are generally consistent with the experimental measurements by Thomas et al.;⁶⁴ however, direct comparison with their data is not possible, because of differences in systems and particle properties. As the gas flow rate increases, the abrupt drop at the impact gets smaller until it virtually vanishes (as does a sudden increase in the stress at the plate (σ_{plate})), and the pressure drop curve during a cycle approaches almost the same, asymptotic sinusoidal curve.

When the vertical component of the stress at the plate is combined with the pressure drop for each case, the resulting curves for different gas flow rates virtually coincide with the same sinusoidal curve (see the inset in the bottom panel of Figure 7). This can be understood from the following force balance relation in the direction of gravity:

$$\frac{\sigma_{\text{plate}}}{\Sigma mg} + \frac{\Delta p}{\Sigma mg} = \frac{g_{\text{eff}}}{g} \quad (17)$$

where Σmg is the weight of the bed per unit cross-sectional area, and the restoring force due to the softness of the particles (i.e., the spring stiffness) is neglected. The above relation holds at every moment during a cycle, and the asymptotic common sinusoidal curve in the inset is identified to be $1 + \Gamma \sin(2\pi ft)$. It corresponds to the effective gravity in the vibrating plate frame (g_{eff}/g ; see the right-hand side of eq 17). Using the fact that the pressure drop across the bed is limited by $(1 + \Gamma)\Sigma mg$ during a cycle, we can examine the validity of the incompressibility assumption for the gas phase that we use. By making use of the equation of state for an ideal gas, one can show that the ratio of the change in gas-phase density $\Delta \rho_g$ to its reference value ρ_{ref} satisfies the relation $\Delta \rho_g/\rho_{\text{ref}} \approx \Delta p/P_{\text{atm}} \leq (1 + \Gamma)\Sigma mg/P_{\text{atm}}$, where P_{atm} is the atmospheric pressure. For the beds of fine powders considered in our study, $\Sigma mg/P_{\text{atm}} \approx \mathcal{O}(10^{-5})$; hence, $\Delta \rho_g/\rho_{\text{ref}} \ll 1$ and the assumption of the incompressibility is valid at every moment during a cycle.

To test the sensitivity of the results to the spring stiffness, we repeated the calculations shown in Figure 7 with an order-of-magnitude-larger value of k_n . The results are presented in Figure 8. The detailed behavior during a cycle is surely dependent on the value of the spring stiffness; the beds of softer particles in Figure 7 noticeably further compress and expand during the impact, and the pressure drop continues to decrease to even below zero during the impact. This effect diminishes when a larger value is used for k_n ; despite the quantitative changes that are readily apparent, the results shown in Figures 7 and 8 are qualitatively similar. Importantly, in a fully fluidized state, pressure pulsation is the only relevant mechanism in both cases, and the value of k_n becomes irrelevant.

Viewing the pressure pulsation at the bottom plate as a forcing set up by the plate, one can inquire about the speed at which this pulsation propagates upward through the bed. Because we have considered the gas phase to be incompressible, the pulse propagates almost instantaneously. Thus, at each time instant, the gas pressure decreases essentially monotonically as one moves up through the bed (except for the small periodic variation associated with the voidage waves). If one allows the

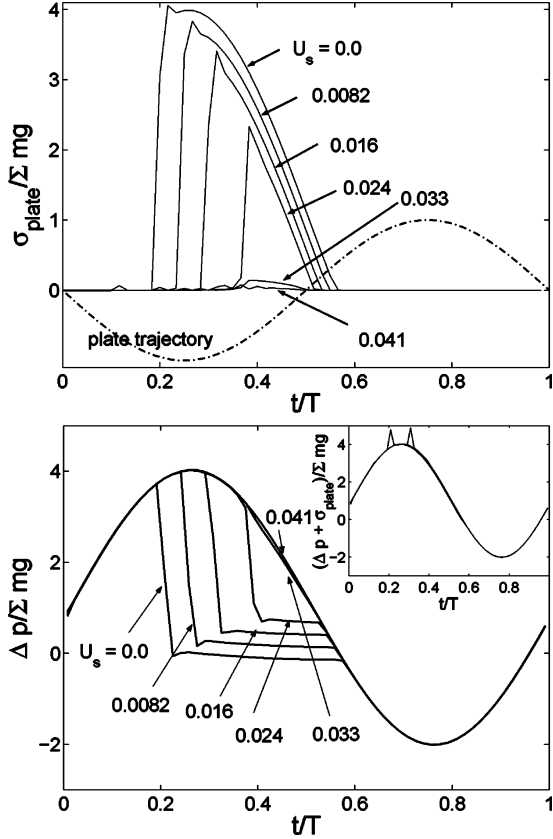


Figure 8. Same quantities measured for the same cases in Figure 7, except that the spring stiffness (k_n and k_s) values have been increased by a factor of 10 (e.g., $k_n = 2.0 \times 10^6$).

gas to be compressible, then the pulsation travels at the speed of sound; sound speed through gas-fluidized beds is considerably smaller than that through a column of gas.⁶⁵ If the time required for the propagation of the pulsation through the bed is commensurate with the period of the plate oscillation, resonance can set in; however, such resonance is suppressed in the present study because we have treated the gas as incompressible. In any case, in the relatively shallow beds that we consider, resonance is not expected to be a significant effect.

The pressure drop averaged throughout a cycle, as a function of gas flow rate, manifests a linear increase up to the constant plateau region (Figure 9), which is qualitatively the same as in conventional fluidized beds. The minimum velocity when the direct impact virtually does not occur is essentially the same as the minimum fluidization velocity in vibrated beds; only the pressure pulsation is a relevant mechanism for a fluidized state of vibrated beds. Note that the minimum fluidization velocities for the vibrated beds of cohesive particles are larger than that for a nonvibrated bed of noncohesive particles of the same size. This can be interpreted as the increment in effective particle size, which is understandable, because the fluidized entities in vibrated beds of cohesive particles are agglomerates, not individual particles. The average volume fraction at the minimum fluidization is smaller (e.g., $\phi_{\text{mf}} = 0.631$ for the case of $Bo = 40$), compared to what is observed in a bed of noncohesive particles ($\phi_{\text{mf}} = 0.652$); cohesive beds have a tendency to pack more loosely. In the fully fluidized state, the pressure drop exhibits a plateau, which approximately equals the weight of the bed per unit cross-sectional area (see Figure 9), as in nonvibrated beds. There is no clear consensus on this issue in experimental studies. Tasirin and Anuar²⁹ reported the pressure drop increases as the vibration intensity Γ increases, Erdész and Mujumdar²⁸ observed the opposite trend, and Marring et al.,⁷

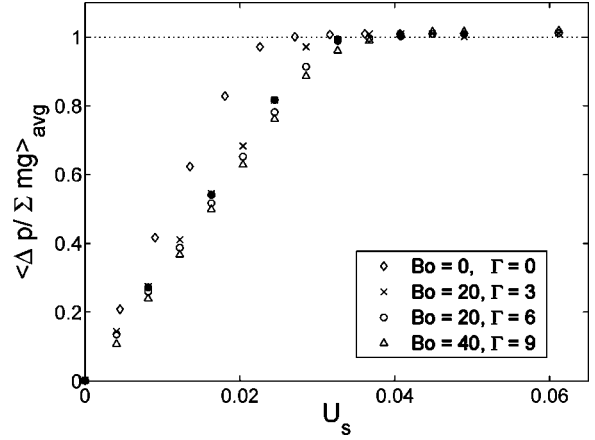


Figure 9. Average pressure drop during a cycle, scaled by the bed weight per unit cross-sectional area, obtained for different cases of vibrated fluidized beds, as a function of U_s . The pressure drop in conventional fluidized beds of noncohesive particles (diamonds) is included for comparison. Filled circles are for the case of $Bo = 20$ and $\Gamma = 3.0$, but the value of spring stiffness that was used ($k_n = 2.0 \times 10^6$) is 10 times larger, compared to all the other cases ($k_n = 2.0 \times 10^5$).

Mawatari et al.,⁹ and Nam et al.¹¹ observed that the constant plateau pressure drop was equal to the bed weight per unit cross-sectional area in high gas flow rates. Only the latter is consistent with our results, which can be explained by the simple force balance argument in eq 17, accounting for the fact that the direct impact is negligibly small in a fluidized state.

3.5. Breakup of Cohesive Assembly by Pressure Pulsation.

We seek to understand how vibration facilitates the breakup of cohesive assemblies into agglomerates and maintains the propagation of the wave in a fluidized state. We analyze the profile of continuum variables, including the granular temperature T and the solid-phase stress tensor σ (or the solid phase pressure) across the traveling wave during a cycle. Because the waves in a bed of finite depth that we have considered thus far are not perfectly periodic, we consider an alternate, idealized geometry, where a wave is fully developed in a small periodic box (in all of three directions) of height L that is commensurate with the wavelength obtained in the vibrated fluidized bed simulations described above. Note that the direct impact does not have an important role for a fully fluidized bed (see section 3.3; only the pressure pulsation has an important role), and the vibrating plate does not have to be considered in such a case. For a fully fluidized state, the weight of the bed per unit cross sectional area is supported by the pressure drop:

$$p|_{z=0} - p|_{z=L} = \rho_p g_{\text{eff}} \phi_{\text{avg}} L \quad (18)$$

where ϕ_{avg} is the average volume fraction.

Comparison between fully fluidized states of cohesive beds and noncohesive beds on microscopic level reveals that cohesive particles form strings of particles or agglomerates while they rain down through void regions, whereas noncohesive particles come down individually (see Figure 10; full animations are available from http://multiphase.princeton.edu/ICE_2005). As one can readily see, this effect arises from the attractive force between cohesive particles, which can be well-characterized by tensile stress on a continuum level. We compute the stress tensor, which consists of a kinetic or dynamic part and a virial or static part, using the following microscopic relation:⁶⁶

$$\sigma = \frac{1}{V} \left[\sum_i m_i \tilde{\mathbf{v}}_i \otimes \tilde{\mathbf{v}}_i - \sum_{c \in V} \mathbf{f}_c \otimes \mathbf{l}_c \right] \quad (19)$$

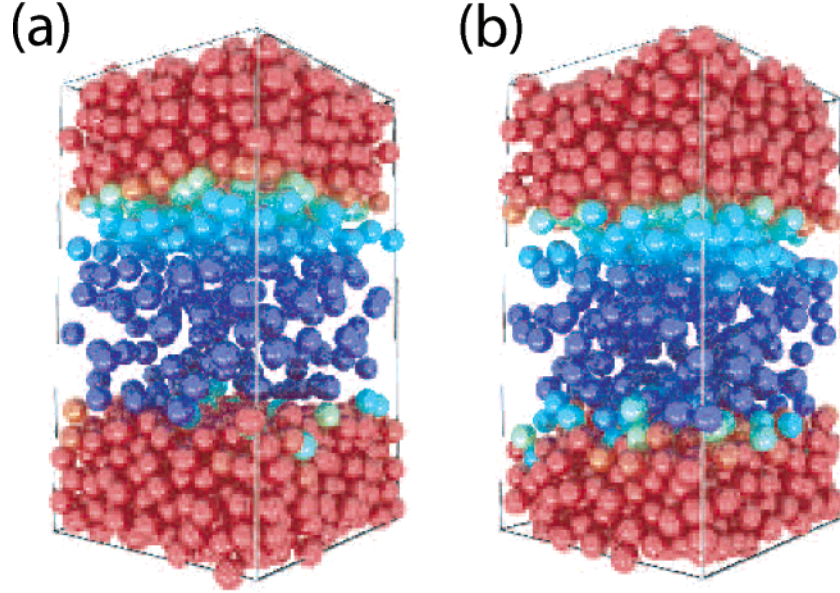


Figure 10. Snapshots of beds of (a) noncohesive particles ($Bo = 0$) and (b) cohesive particles ($Bo = 4$), obtained from particles in a box of height $L = 18d_p$ and cross-sectional area of $10d_p \times 10d_p$ ($\phi_{avg} = 0.40$). Periodic boundary conditions are imposed in all three directions (see text). Particles rain down from the upper plug to the lower plug, while void regions in the middle rise up, which form travelling voidage waves. Note that cohesive particles form strings or agglomerates while they rain down. [Color online: Particles are color-coded according to the vertical velocity, increasing from blue (moving downward) to green to red (moving upward).] Full animations are available via the Internet at http://multiphase.princeton.edu/ICE_2005.

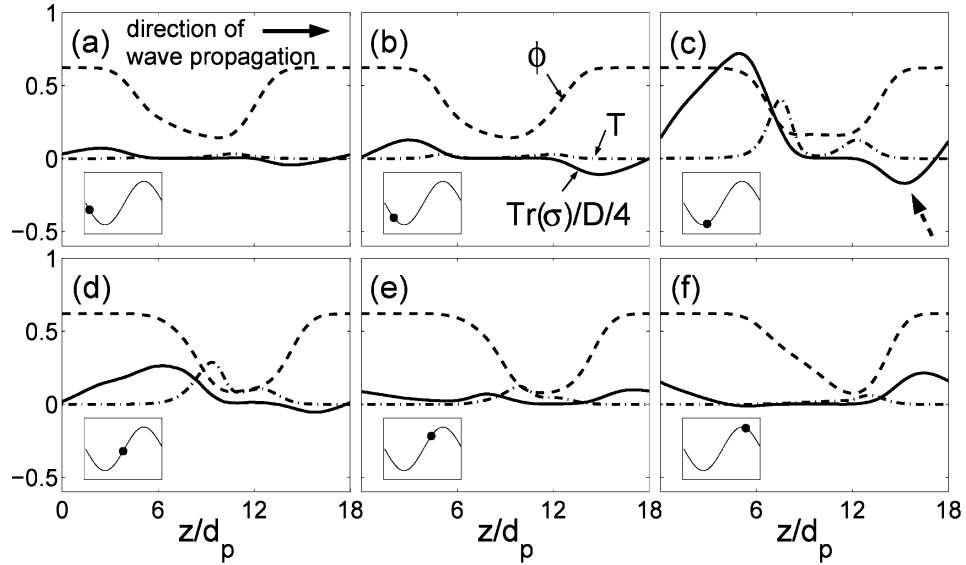


Figure 11. Solid-phase continuum variables of a highly cohesive bed ($Bo = 20$, $\phi_{avg} = 0.40$) during a cycle in the vibrating frame ($\Gamma = 3.0$), obtained in the same geometry as that given in Figure 10. Insets represent the phase angle during a cycle in terms of the vertical location of the (virtually existing) base plate (indicated by dots). The void region in the middle oscillates up and down and has an upward net motion (indicated by a gray arrow in panel a). The solid-phase stress during a cycle can be summarized by the following stages: (a) The pressure pulsation is weak and the particle phase pressure is negligibly small throughout the bed; (b) as the pressure pulsation increases, the magnitude of the normal stress both in compressive (in lower plug) and tensile regions (in upper plug) and the granular temperature also increase; (c) this increase continues until they reach their maximum values, and around this time, the tensile stress reaches the tensile strength of the material, which breaks up the cohesive assembly into agglomerates; (d) the stress then relaxes; and (e and f) a relatively small compressive stress amasses at the bottom of the upper plug, but this is not relevant for the breakup of the assembly. The location of the peak tensile stress is indicated by a broken arrow in panel c. A full animation during two cycles is available via the Internet at http://multiphase.princeton.edu/ICE_2005.

where $\tilde{\mathbf{v}}_i$ is the fluctuating velocity of the i th particle ($\tilde{\mathbf{v}}_i = \mathbf{v}_i - \langle \mathbf{v}_i \rangle$), \otimes is the dyadic tensor product, f_c is the interacting force between contacting particles 1 and 2, and \mathbf{l}_c is the displacement vector between the centers of particles under consideration ($\mathbf{l}_c = \mathbf{r}_1 - \mathbf{r}_2$). The second term is summed over all the contacts in the averaging volume V .

Now we consider the continuum level interpretation of vibrated fluidized beds of highly cohesive particles in a fully periodic box during an oscillation cycle (Figure 11). During a cycle, the wave oscillates up and down with a net upward

motion, as can be seen in the cases shown in Figure 3. We compute the solid-phase continuum variables, including the pressure and the trace of the stress tensor per dimension ($\text{Tr}(\sigma)/D$). We compute them in the co-travelling frame (with the wave's net motion), averaged over 100 cycles, for the purpose of variance reduction. As the pressure pulsation cyclically varies during a cycle, so do both the granular temperature and the stress tensor.

Figure 11 shows the variation of solid-phase continuum variables at six different times during an oscillation cycle. The

inset in each panel shows the position of a hypothetical, oscillating base plate at the instant the profiles of the continuum variables are shown. The plate trajectory sketched in the insets can be compared to that shown in the top panel of Figure 7. The corresponding pressure drop across the periodic domain can be determined from the cyclically varying pressure drop profile in the bottom panel of Figure 7, which is almost out of phase with the plate position. In Figure 11a, the value of g_{eff}/g and the scaled pressure drop are almost unity; they are larger in Figure 11b, attain their largest values near the instant shown in Figure 11c, relax back toward unity in Figure 11d, and then they decrease in Figure 11e, until they reach the minimum values in Figure 11f.

When the scaled pressure drop is almost unity (Figure 11a), the solid-phase pressure is negligibly small throughout the bed. As the pressure drop increases until it reaches its maximum value (Figures 11b and c), the granular temperature and compressive stress in the lower plug and tensile stress in the upper plug also increase significantly, until they reach their maximum magnitudes. The large granular temperature occurs at the lower plug, where the particles or agglomerates are accumulated. The phenomenon results from vigorous collisions among the particles or agglomerates that are raining down and the lower plug. Note that the volume fraction in this region is still low (the value of ϕ is less than ~ 0.3). A rough estimate for the magnitude of the stress using the values at the maximum temperature region ($\sim nT = 6/(\pi d_p^3)\phi T \approx 0.2$), where the most vigorous collisions occur, shows that it is still much smaller than the tensile strength of the cohesive assembly (~ 1) that is estimated below; here, n is the number density. In order for these vigorous collisions to contribute to the breakup of the cohesive assembly, the magnitude of the stress formed by the collisions must be comparable or larger than the tensile strength of the material. However, the stresses formed by the collisions are not strong enough to break up the assembly and are irrelevant for the assembly breakup. Rather, it is the increased tensile stress in the upper plug that breaks up the assembly into agglomerates and maintains the wave propagation. Particles in the upper plug can split off from the assembly and rain down, because the increased tensile stress becomes large enough to reach the tensile strength of the cohesive assembly. It occurs at a time near that shown in Figure 11c.

The magnitude of the tensile stress cannot exceed the strength of the assembly; therefore, we estimate the strength of the fluidized bed by measuring the maximum tensile stress. We compare such obtained tensile strength of the fluidized bed with the prediction of Rumpf's model,⁶⁷

$$\sigma_t = \left(\frac{1 - \epsilon}{\pi} \right) k \left(\frac{F_t}{d_p} \right) \quad (20)$$

where σ_t is the tensile strength, ϵ the porosity ($\epsilon = 1 - \phi$), k the coordination number, and F_t the cohesive contact force. We find that our measurement ($\sigma_t \approx 0.8$) is approximately an order of magnitude smaller than the prediction ($\sigma_t \approx 6$). This discrepancy is understandable, because the cohesive assembly in a fluidized bed breaks up through the weakest linkage, as opposed to all directions, as is assumed in Rumpf's model.

Later in the cycle, when pressure drop decreases and approaches the minimum value (Figure 11d–f), the particle phase pressure is generally small in the bed. When the pressure drop is negative, a relatively small compressive stress amasses at the bottom of the upper plug as the gas in the void region pushes up; this is obviously irrelevant for the breakup.

4. Summary

We have used a particle-dynamics-based model for vibrated gas-fluidized beds of fine powders to study how the vibration facilitates the fluidization of beds of cohesive powders. We have demonstrated that, as the gas flow rate increases, the direct impact from the plate decreases and the pressure pulsation becomes more dominant. In a fluidized state, the latter is shown to be virtually the only relevant mechanism, and the pressure drop follows a simple sinusoidal curve during a cycle (see Figures 7 and 8), which corresponds to the weight of the bed per unit cross-sectional area in the vibrated frame. As a consequence, the pressure drop averaged over a cycle in the fluidized state is simply the offset of this sinusoidal curve, which equals the weight of the bed per unit cross-sectional area, as in nonvibrated beds. This relation can be readily understood by a simple force balance argument (see eq 17). In a bubbling bed (which appears as 1D-TW in our study), it is during the transient time interval with large enough pressure pulsation when the increased tensile stress breaks up the cohesive assembly into agglomerates (see Figure 11).

Note that the compressibility of the gas phase was ignored in the present study; it would be interesting to investigate the resonance effects that may arise in vibrated beds by allowing for gas compressibility. It was also assumed that the gas superficial velocity is independent of time throughout the oscillation cycle, and this corresponds to the limit of very large resistance for gas flow through the distributor; it would also be interesting to examine the case of finite distributor resistance, where the superficial gas velocity can be expected to vary cyclically with plate vibration.

While the present study has yielded a physical understanding of the pressure fluctuations induced by the plate and the tensile stress in the particle assembly, an analytical relation between vibration parameters and the agglomerate size is still elusive. Furthermore, we have considered only beds of narrow cross-sectional areas, and we have assumed the volume-averaged gas phase to be one-dimensional. Consequently, some generic behavior in real vibrated gas-fluidized beds, such as the horizontal sloshing motion of the particles, meandering gas flows around agglomerates, and more complicated bubble dynamics, were not allowed to occur. By avoiding such complexity, we were able to bring out certain basic physics of the bed dynamics. Future studies should investigate the dynamics of higher-dimensional beds; however, simulation of fluidized beds of realistic industrial scales, using the current approach, is not yet feasible.

Acknowledgment

This work was funded by The New Jersey Commission on Science and Technology, Merck & Co., Inc., and an NSF/ITR grant. We are delighted to contribute this article to the special issue honoring W. B. Russel. Having him as a colleague and a friend has been a pleasure and a privilege for both S.S. and I.G.K. We salute his accomplishments and look forward to many more years of work and fun together.

Nomenclature

- A = Hamaker constant
- Bo = cohesive Bond number between particles
- Bo_p = cohesive Bond number between particles and the base plate
- C_D = drag coefficient
- Δp = pressure drop across the bed

Δz = grid spacing for coarse-grained variables
 d_p = particle diameter
 e = normal coefficient of restitution
 f = vibration frequency
 F_{cont} = interaction force due to contact
 F_c = cohesive force due to van der Waals force
 g_{eff} = effective gravitational acceleration
 h = halo function
 k = coordination number
 k_n = spring stiffness in the normal direction
 k_t = spring stiffness in the tangential direction
 m_p = mass of individual particle
 n = solid-phase number density
 P_{atm} = atmospheric pressure
 p = gas-phase pressure
 Re_g = Reynolds number based on particle size
 r = particle radius
 s = intersurface distance
 St = Stokes number
 T = granular temperature
 Σmg = bed weight per unit cross-sectional area
 u_g = volume-averaged gas-phase velocity
 u_s = volume-averaged solid-phase velocity
 U_s = superficial gas-flow velocity
 U_{mf} = minimum fluidization velocity
 v_n = relative velocity in the normal direction
 v_s = relative velocity in the tangential direction
 v_p = velocity of an individual particle
 V_p = volume of an individual particle

Greek Symbols

β = interphase momentum transfer
 δ, δ^* = minimum separation distance for cohesion
 Δ_s = tangential displacement from initial contact
 Δ_n = amount of overlap in the normal direction
 ϵ = porosity (gas-phase volume fraction)
 ϕ = solid-phase volume fraction
 γ_n = damping coefficient for dashpot
 Γ = vibration intensity
 μ = coefficient of friction
 μ_g = gas-phase viscosity
 ν_p = Poisson's ratio
 ρ_g = gas-phase mass density
 ρ_s = solid-phase mass density
 σ = solid-phase stress tensor
 σ_t = tensile strength of the material
 σ_{plate} = vertical stress on the plate

Literature Cited

- (1) Geldart, D. Types of gas fluidization. *Powder Technol.* **1973**, 7, 285–292.
- (2) Visser, J. An Invited Review: van der Waals and Other Cohesive Forces Affecting Powder Fluidization. *Powder Technol.* **1989**, 58, 1–10.
- (3) Mohan, M. R.; Dave, R. N.; Pfeffer, R. Promotion of deactivated sintering by dry-particle coating. *AIChE J.* **2004**, 49 (3), 604–618.
- (4) Ferguson, J. D.; Weimer, A. W.; George, S. M. Atomic layer deposition of ultrathin and conformal Al_2O_3 films on BN particles. *Thin Solid Films* **2000**, 371, 95–104.
- (5) Dutta, A.; Dullea, L. V. Effects of External Vibration and the Addition of Fibers on the Fluidization of a Fine Powder. *AIChE Symp. Ser.* **1991**, 87, 38.
- (6) Jaraiz, E.; Kimura, S.; Levenspiel, O. Vibrating beds of fine particles: estimation of interparticle forces from expansion and pressure drop experiments. *Powder Technol.* **1992**, 72, 23–30.
- (7) Maring, E.; Hoffmann, A. C.; Janssen, L. P. B. M. The effect of vibration on the fluidization behavior of some cohesive powders. *Powder Technol.* **1994**, 79, 1–10.
- (8) Wank, J. R.; George, S. M.; Weimer, A. W. Vibro-fluidization of fine boron nitride powder at low pressure. *Powder Technol.* **2001**, 121, 195–203.
- (9) Mawatari, Y.; Koide, T.; Tatemoto, Y.; Uchida, S.; Noda, K. Effect of particle diameter on fluidization under vibration. *Powder Technol.* **2002**, 123, 69–74.
- (10) Mawatari, Y.; Tatemoto, Y.; Noda, N. Prediction of minimum fluidization velocity for vibrated fluidized bed. *Powder Technol.* **2003**, 131, 66–70.
- (11) Nam, C. H.; Pfeffer, R.; Dave, R. N.; Sundaresan, S. Aerated Vibrofluidization of Silica Nanoparticles. *AIChE J.* **2004**, 50, 1776–1785.
- (12) Valverde, J. M.; Castellanos, A.; Quintanilla, M. A. S. Effect of vibration on the stability of a gas-fluidized bed of fine powder. *Phys. Rev. E* **2001**, 64, 021302/1–021302/8.
- (13) Chirone, R.; Massimilla, L.; Russo, S. Bubble-free fluidization of a cohesive powder in an acoustic field. *Chem. Eng. Sci.* **1993**, 48, 41–52.
- (14) Nowak, W.; Hasatani, M. Fluidization and heat transfer of fine particles in an acoustic field. *AIChE Symp. Ser.* **1993**, 89, 137.
- (15) Russo, P.; Chirone, R.; Massimilla, L.; Russo, S. The influence of the frequency of acoustic waves on sound-assisted fluidization of fine particles. *Powder Technol.* **1995**, 82, 219–230.
- (16) Yu, Q.; Dave, R. N.; Zhu, C.; Quevedo, J. A.; Pfeffer, R. Enhanced fluidization of nanoparticles in an oscillating magnetic field. *AIChE J.* **2005**, 51 (7), 1971–1979.
- (17) Melo, F.; Umbanhowar, P. B.; Swinney, H. L. Transition to parametric wave patterns in a vertically oscillated granular layer. *Phys. Rev. Lett.* **1994**, 72, 172–175.
- (18) Umbanhowar, P. B.; Melo, F.; Swinney, H. L. Localized excitations in a vertically vibrated granular layer. *Nature* **1996**, 382, 793–796.
- (19) Möbius, M. E.; Lauderdale, B. E.; Nagel, S. R.; Jaeger, H. M. Brazil-nut effect: Size separation of granular particles. *Nature* **2001**, 414, 270.
- (20) Burtally, N.; King, P. J.; Swift, M. R. Spontaneous Air-Driven Separation in Vertically Vibrated Fine Granular Mixtures. *Science* **2002**, 295, 1877–1879.
- (21) Moon, S. J.; Goldman, D. I.; Swift, J. B.; Swinney, H. L. Kink-induced transport and segregation in oscillated granular layers. *Phys. Rev. Lett.* **2003**, 91, 134301.
- (22) Hong, D. C.; Quinn, P. V.; Luding, S. Reverse Brazil Nut Problem: Competition between Percolation and Condensation. *Phys. Rev. Lett.* **2001**, 86, 3423–3426.
- (23) Naylor, M. A.; Swift, M. R.; King, P. J. Air-driven Brazil nut effect. *Phys. Rev. E* **2003**, 68, 012301.
- (24) Möbius, M. E.; Cheng, X.; Eshuis, P.; Karczmar, G. S.; Nagel, S. R.; Jaeger, H. M. Effect of air on granular size separation in a vibrated granular bed. *Phys. Rev. E* **2005**, 72, 011304.
- (25) Squires, A. M. Chemical process opportunities for vibrated powders: 2. In the field. *Powder Technol.* **2004**, 147, 10–19.
- (26) Musters, S. M. P.; Rietema, K. The effect of interparticle forces on the expansion of a homogeneous gas-fluidized bed. *Powder Technol.* **1977**, 18, 239–248.
- (27) Liss, B. Incipient defluidization of sinterable solids. In *Fluidization*; American Institute of Chemical Engineers (AIChE): New York, 1983; pp 249–256.
- (28) Erdész, K.; Mujumdar, A. S. Hydrodynamic Aspects of Conventional and Vibrofluidized Beds—A Comparative Evaluation. *Powder Technol.* **1986**, 46, 167–172.
- (29) Tasirin, S. M.; Anuar, N. Fluidization Behavior of Vibrated and Aerated Beds of Starch Powders. *J. Chem. Eng. Jpn.* **2001**, 34, 1251–1258.
- (30) Fan, L. S.; Zhu, C. *Principles of Gas–Solid Flows*; Cambridge University Press: Cambridge, U.K., 1998.
- (31) Gidaspow, D. *Multiphase Flow and Fluidization: Continuum and Kinetic Theory Description*; Academic Press: Boston, 1994.
- (32) Jackson, R. *The Dynamics of Fluidized Particles*; Cambridge University Press: Cambridge, U.K., 2000.
- (33) Cundall, P. A.; Strack, O. D. L. A discrete numerical model for granular assemblies. *Geotechnique* **1979**, 29, 47–65.
- (34) Tsuji, Y.; Kawaguchi, T.; Tanaka, T. Discrete particle simulation of two-dimensional fluidized bed. *Powder Technol.* **1993**, 77, 79–87.
- (35) Hoomans, B. P. B.; Kuipers, J. A. M.; Briels, W. J.; van Swaaij, W. P. M. Discrete particle simulation of bubble and slug formation in a two-dimensional gas-fluidized bed: A hard-sphere approach. *Chem. Eng. Sci.* **1996**, 51, 99–118.
- (36) Xu, B. H.; Yu, A. B. Numerical simulation of the gas-particle flow in a fluidized bed by combining discrete particle method with computational fluid dynamics. *Chem. Eng. Sci.* **1997**, 52, 2785–2809.

- (37) Ye, M.; van der Hoef, M. A.; Kuipers, J. A. M. A numerical study of fluidization behavior of Geldart A particles using a discrete particle simulation. *Powder Technol.* **2004**, *139*, 129–139.
- (38) Rhodes, M. J.; Wang, X. S.; Nguyen, M.; Stewart, P.; Liffman, K. Use of discrete element method simulation in studying fluidization characteristics: Influence of interparticle force. *Chem. Eng. Sci.* **2001**, *56*, 69–76.
- (39) Rhodes, M. J.; Wang, X. S.; Nguyen, M.; Stewart, P.; Liffman, K. Onset of cohesive behaviour in gas fluidized beds: A numerical study using DEM simulation. *Chem. Eng. Sci.* **2001**, *56*, 4433–4438.
- (40) Bokkers, G. A.; van Sint Annaland, M.; Kuipers, J. A. M. Mixing and segregation in a bidisperse gas-solid fluidised bed: A numerical and experimental study. *Powder Technol.* **2004**, *140*, 176–186.
- (41) Zhu, H. P.; Yu, A. B. Steady-state granular flow in a three-dimensional cylindrical hopper with flat bottom: microscopic analysis. *J. Phys. D: Appl. Phys.* **2004**, *37*, 1497–1508.
- (42) Volfson, D.; Tsimring, L. S.; Aranson, I. S. Partially fluidized shear granular flows: Continuum theory and molecular dynamics simulations. *Phys. Rev. E* **2003**, *68*, 021301.
- (43) McCarthy, J. J.; Shinbrot, T.; Metcalfe, G.; Wolf, D. E.; Ottino, J. M. Mixing of granular materials in slowly rotated containers. *AIChE J.* **1996**, *42*, 3351–3363.
- (44) Mehta, A.; Barker, G. C. Vibrated powders: A microscopic approach. *Phys. Rev. Lett.* **1991**, *67*, 394–397.
- (45) Wassgren, C. R. Vibration of granular materials, Ph.D. dissertation, California Institute of Technology, Pasadena, CA, 1997.
- (46) Herrmann, H. J.; Luding, S. Review Article: Modeling granular media with the computer. *Continuum Mech. Thermodyn.* **1998**, *10*, 189–231.
- (47) Duran, J. *Sands, Powders, and Grains: An Introduction to the Physics of Granular Materials*; Springer-Verlag: New York, 2000.
- (48) Rapaport, D. C. *The Art of Molecular Dynamics Simulation*; Cambridge University Press: Cambridge, U.K., 2004.
- (49) Walton, O. R.; Braun, R. L. Viscosity, granular temperature, and stress calculations for shearing assemblies of inelastic, frictional disks. *J. Rheol. (N.Y.)* **1986**, *30*, 949–980.
- (50) Schäfer, J.; Dippel, S.; Wolf, D. E. Force Schemes in Simulations of Granular Materials. *J. Phys. I* **1996**, *6*, 5–15.
- (51) Israelachvili, J. N. *Intermolecular and Surface Forces*; Academic Press: London, 1997.
- (52) Seville, J. P. K.; Willett, C. D.; Knight, P. C. Interparticle forces in fluidization: A review. *Powder Technol.* **2000**, *113*, 261–268.
- (53) Kuwagi, K.; Horio, M. A numerical study on agglomerate formation in a fluidized bed of fine cohesive particles. *Chem. Eng. Sci.* **2002**, *57*, 4737–4744.
- (54) Mikami, T.; Kamiya, H.; Horio, M. Numerical simulation of cohesive powder behavior in a fluidized bed. *Chem. Eng. Sci.* **1998**, *53*, 1927–1940.
- (55) Wen, C. Y.; Yu, Y. H. Mechanics of fluidization. *Chem. Eng. Prog. Symp. Ser.* **1966**, *62*, 100–111.
- (56) Rowe, P. N. Drag forces in a hydraulic model of a fluidized bed: II. *Trans. Inst. Chem. Eng.* **1961**, *39*, 175–180.
- (57) Davidson, J. F.; Clift, R.; Harrison, D., Eds. *Fluidization*, 2nd Edition; Academic Press: London, 1985.
- (58) Glasser, B. J.; Kevrekidis, I. G.; Sundaresan, S. One- and two-dimensional traveling wave solutions in gas-fluidized beds. *J. Fluid Mech.* **1996**, *306*, 183–221.
- (59) Glasser, B. J.; Sundaresan, S.; Kevrekidis, I. G. From Bubbles to Clusters in Fluidized Beds. *Phys. Rev. Lett.* **1998**, *81*, 1849–1852.
- (60) Sundaresan, S. Instabilities in fluidized beds. *Annu. Rev. Fluid Mech.* **2003**, *35*, 63–88.
- (61) Mehta, A.; Luck, J. M. Novel temporal behavior of a nonlinear dynamical system: The completely inelastic bouncing ball. *Phys. Rev. Lett.* **1990**, *65*, 393–396.
- (62) Moon, S. J.; Shattuck, M. D.; Bizon, C.; Goldman, D. I.; Swift, J. B.; Swinney, H. L. Phase bubbles and spatiotemporal chaos in granular patterns. *Phys. Rev. E* **2002**, *65*, 011301.
- (63) Umbanhowar, P. B. Wave Patterns in Vibrated Granular Layers, Ph.D. dissertation, The University of Texas at Austin, Austin, TX, 1996.
- (64) Thomas, B.; Mason, M. O.; Squires, A. M. Some behaviors of shallow vibrated beds across a wide range in particle size and their implications for powder classification. *Powder Technol.* **2000**, *111*, 34–49.
- (65) Gregor, W.; Rumpf, H. Velocity of sound in two-phase media. *Int. J. Multiphase Flow* **1975**, *1*, 753–769.
- (66) Lätzel, M.; Luding, S.; Herrmann, H. J. Macroscopic material properties from quasi-static, microscopic simulations of a two-dimensional shear-cell. *Granular Matter* **2000**, *2* (3), 123–135.
- (67) Rumpf, H. The strength of granules and agglomerates. In *Agglomeration*; Knepper, W. A., Ed.; Interscience: New York, 1962.

Received for review October 5, 2005
 Revised manuscript received January 10, 2006
 Accepted January 11, 2006

IE051114S